Formation and Near-infrared Emission of $CsPbI_3$ Nanoparticles Embedded in Cs_4PbI_6 Crystals

Zhen Bao[1†], Chiao-Yin Hsiu[1†], Mu-Huai Fang[1], Natalia Majewska[2], Weihao Sun[3], Shing-Jong Huang[4], Eric Chung-Yueh Yuan [1], Yu-Chun Chang[1], Jerry Chun Chung Chan[1], Sebastian Mahlik[2], Wuzong Zhou[3], Chia-Wei Yang[5], Kuang-Mao Lu[5], & Ru-Shi Liu[1,6]**

[1]Department of Chemistry, National Taiwan University, Taipei 106, Taiwan

[2]Institute of Experimental Physics, Faculty of Mathematics, Physics and Informatics, University of Gdańsk, Gdańsk 80-308, Poland

[3]School of Chemistry, University of St Andrews, St Andrews KY16 9ST, United Kingdom

[4]Instrumentation Center, National Taiwan University, Taipei 106, Taiwan

[5]Everlight Electronics Co., Ltd., New Taipei City 238, Taiwan

[6]Advanced Research Center of Green Materials Science and Technology, National Taiwan University, Taipei 106, Taiwan

[†]Zhen Bao and Chiao-Yin Hsiu contributed equally to this work.

Corresponding Authors

wzhou@st-andrews.ac.uk (W. Z. Zhou)

rsliu@ntu.edu.tw (R. S. Liu)

Keywords: Cs_4PbI_6; perovskite; crystals; near-infrared; $CsPbI_3$; electron microscopy; embedded nanoparticles.

ABSTRACT

Cs_4PbI_6, as a rarely investigated member of the Cs_4PbX_6 (X is a halogen element) family, has been successfully synthesized at low temperatures, and the synthetic conditions have been optimized. Metal iodides such as LiI, KI, NiI_2, CoI_2, and ZnI_2, as additives, play an important role in enhancing the formation of the Cs_4PbI_6 microcrystals. ZnI_2 with the lowest dissociation energy is the most efficient additive to supply iodide ions, and its amount of addition has also been optimized. Strong red to near-infrared (NIR) emission properties have been detected, and its optical emission centers have been identified to be numerous embedded perovskite-type α-$CsPbI_3$ nanocrystallites (~5 nm in diameter) based on investigations of temperature- and pressure-dependent photoluminescent properties. High-resolution transmission electron microscopy was used to detect these hidden nanoparticles, although the material was highly beam-sensitive and confirmed a 'raisin bread'-like structure of the Cs_4PbI_6 crystals. A NIR mini-LED for the biological application has been successfully fabricated using as-synthesized Cs_4PbI_6 crystals. This work provides information for the future development of infrared fluorescent nanoscale perovskite materials.

INTRODUCTION

All-inorganic perovskite has potential in various applications, such as solar cells,[1-2] light-emitting diodes (LEDs),[3-5] and photodetectors.[6-7] $CsPbX_3$ (X = Cl, Br, I) crystals have been paid increasing attention because of their unique photoluminescence properties. However, normal-sized $CsPbX_3$ crystals lack stability, thus limiting their commercial applications.[8,9-12] Consequently, zero-dimensional perovskite, which has surface protection and improved stability without ion-migration phenomenon, has attracted the attention of researchers worldwide. Considering their excellent optical properties, such as narrowband emission,[11] high photoluminescence quantum yield (PLQY),[13] and better stability than normal-sized materials,[11] zero-dimensional perovskite-type materials have been considered as promising materials for applications in LEDs. Many research groups have attempted to apply Cs_4PbBr_6 perovskite-related microcrystals or perovskite $CsPbBr_3$ nanocrystal (NC)-embedded Cs_4PbBr_6 crystals to improve the color gamut of white LEDs for backlight.[10, 13-17] Although LEDs based on Cs_4PbBr_6 have been developed quite fast, reports on the applications of perovskite-type materials in near-infrared (NIR) LEDs are relatively rare.

The iodide counterpart may offer another chance in the field in question. The first problem we encountered was that the synthesis of monophasic Cs_4PbI_6 was very difficult. By comparing the emission mechanism of the $CsPbBr_3$-containing Cs_4PbBr_6 microcrystals, the luminescent Cs_4PbI_6 may also contain embedded $CsPbI_3$ nanoparticles as the emission centers.[18] Therefore, whether the hypothetical structure of $CsPbI_3$-containing Cs_4PbI_6 exists will be the key to reveal the origin of the emission. However, the Cs–Pb–I system consists of more compounds than that of the Cs–Pb–Br system. The luminescent cubic $CsPbI_3$ with a perovskite structure, commonly known as α-$CsPbI_3$, is unstable at room temperature. It will easily transform to a non-perovskite orthorhombic structure, known as δ-$CsPbI_3$,[19-20], leaving some difficulties in the study of the

luminescence mechanism of the Cs_4PbI_6. Hence, the main challenges of the project include keeping the luminescent α-$CsPbI_3$ nanoparticles stably embedded in the Cs_4PbI_6 microcrystals and avoiding the formation of side products. To maximize the purity of the Cs_4PbI_6 product with embedded perovskite α-$CsPbI_3$, the formation of δ-$CsPbI_3$ is inhibited at high temperatures, and this material normally exists as separated crystals from Cs_4PbI_6.[21-23] However, the room-temperature process for the fabrication of $CsPbI_3$-embedded Cs_4PbI_6 has not been extensively investigated. Furthermore, most recent reports on Cs_4PbI_6 are mainly focused on the phase transition kinetics and process.[19, 24-26] Only Zhu *et al.*[27] gave an explanation of the defect emission process, but it is doubt about the strong emission from Cs_4PbI_6. The luminescent properties of these materials are rarely discussed, and the emission mechanism of the materials remains to be determined for future application.

In this work, we successfully optimized the low-temperature synthesis process for the red-near-infrared (NIR) fluorescent α-$CsPbI_3$-embedded Cs_4PbI_6. We infer that the strongest NIR emission originates from the embedded α-$CsPbI_3$ nanoparticles according to the temperature- and pressure-dependent photoluminescence (PL) spectra.

EXPERIMENTAL SECTION

Chemicals and substrates. All chemicals were used without purification, including cesium carbonate (Cs_2CO_3, Aldrich, 99.9%), lead iodide (PbI_2, ABCR, 98%), zinc(II) iodide (ZnI_2, Alfa, 99.2%), 1-octadecene (ODE, Aldrich, 90%), oleic acid (OA, Sigma-Aldrich, 90%), oleylamine (OAm, Acros Organics, 80%–90%), hydriodic acid (HBr, Alfa Aesar, 55~58% *w*/*w* aq. soln.), and N, N-Dimethylformamide (DMF, for HPLC).

Preparation of Cs-oleate precursor. Exactly 3.4 mmol Cs_2CO_3 was mixed with 10 mL of OA in a 50 mL three-neck flask. The mixture was heated to 130 °C for degassing and dried in vacuo at 130 °C for 1 h. The Cs-oleate precursor solution was stored in a three-neck flask under N_2 for the later synthesis of perovskite crystals.

Synthesis of Cs_4PbI_6 with different amounts of additive ZnI_2. First, 10 mL of toluene, 5 mL of OA, and 1 mL of prepared Cs-oleate precursor were loaded in a 50-mL three-neck flask under the nitrogen. Then, a mixture of $0.3(1–x)$ mmol PbI_2, $0.3x$ mmol ZnI_2 (x = 0 to 1), 1 mL DMF, 15 μL HI, 0.5 mL OA, and 0.5 mL OAm was injected under 400 rpm stirring. After stirring for 30 min, the green crystals were centrifuged at 5,000 rpm for 6 min for collection. The powder was finally stored in 5 mL of toluene.

Synthesis of Cs_4PbI_6 with different OAm/OA ratios. In this procedure, OA and OAm were controlled for the total amount of 1 mL. First, 10 mL of toluene, y mL of OA (y = 0 to 1), and 1 mL of Cs–oleate precursor were loaded in a 50-mL three-neck flask under a nitrogen atmosphere. Then, a mixture of $0.3(1–x)$ mmol PbI_2, $0.3x$ mmol ZnI_2 (x = 0 to 1), 1 mL DMF, 15 μL HI, 0.5 mL OA, and $1–y$ mL OAm was injected under 400 rpm stirring. After stirring for 30 min, the green crystals were centrifuged at 5,000 rpm for 6 min for collection. The powder was finally stored in 5 mL of toluene.

Synthesis of Cs_4PbI_6 perovskite with different additional MI_2 salt. First, 10 mL of toluene, 5 mL of OA, and 1 mL of Cs-oleate precursor were loaded in a 50-mL three-neck flask under the nitrogen. Then, a mixture of $0.3(1–x)$ mmol PbI_2, $0.3x$ mmol MI_2 (x = 0 to 1), 1 mL DMF, 15 μL HI, 0.5 mL OA, and 0.5 mL OAm was injected under 400 rpm stirring. After stirring for 30 min, the green crystals were centrifuged at 5,000 rpm for 6 min for collection. The powder was finally stored in 5 mL toluene.

Structure Characterization. The obtained Cs_4PbI_6 specimens were initially characterized using X-ray diffraction (XRD) in the National Synchrotron Radiation Research Centre, Hsinchu, Taiwan. Scanning electron microscopy (SEM) images and energy-dispersive X-ray spectrometry (EDS) elemental mapping of the Cs_4PbI_6 crystals were recorded on a ZEISS Σ SIGMA essential scanning electron microscope. High resolution transmission electron microscopy (HRTEM) images were recorded on a scanning transmission electron microscope (Titan Themis 200). The operation voltage was 200 kV. The powder sample was ground and dispersed in acetone before being deposited on a TEM specimen grid with a holey carbon film for the TEM observation. TEM data were analyzed using Gatan digital micrograph. ^{133}Cs MAS NMR spectra were acquired on a wide-bore 14.1-T Bruker Avance III spectrometer equipped with a 4-mm MAS double-resonance probe head at a Larmor frequency of 78.72 MHz. The excitation pulse width was 0.5 μs with an rf nutation field of 40 kHz, and the recycle delay was set to 6 s. The sample spinning rate was 14.5 kHz. The ^{133}Cs chemical shifts were externally referenced to 0.1 M $CsNO_3$ in D_2O.

Temperature- and pressure-dependent PL. Room temperature photoluminescence excitation RT PLE and PL spectra were obtained on a FluoroMax-4P spectrofluorometer (Horiba) equipped with a 150 W xenon lamp as an excitation source and an R928 Hamamatsu photomultiplier as a detector, which allowed the recording of PL and PLE spectra in the spectral range of 250–850 nm. The temperature and pressure dependence of PL spectra were recorded using an Andor SR-750-D1 spectrometer equipped with a CCD camera (DU420A-OE) and a Kimmon Koha He-Cd laser, at 442 and 325 nm.

The quantum yields was measured by using an absolute PL quantum yield spectrometer (c11347, Hamamatsu). The excitation wavelength was set at 460 nm to simulate the working status of the sample on the InGaN LED chips.

The time-resolved luminescence and decay profiles were measured using an apparatus that consists of a PG 401/SH optical parametric generator pumped by a PL2251A pulsed YAG: Nd laser (EKSPLA). The detection part consists of a 2501S grating spectrometer (Bruker Optics) combined with a C4334-01 streak camera (Hamamatsu). A software-based photon-counting algorithm transformed the result into a 2D matrix of photon counts versus wavelength and time and recorded data in the form of the streak images on a 640 × 480 pixel CCD array. The high-pressure luminescence measurements were performed in a screw-driven Merrill-Bassett type diamond anvil cell with a 0.5 mm diamond culet diameter. The gasket for the pressure chamber was pre-indented to approximately 0.07 mm, and a 0.2 mm-diameter hole was drilled in the center of the gasket indentation. Ruby was used as a pressure sensor, while polydimethylsiloxane oil was used as a pressure transmitting medium.

Fabrication of mini-LEDs and the light penetration experiment. The raisin bread (RB)-like RB-Cs_4PbI_6 perovskite powder was mixed with silicone resin. After bubbles were removed, the mixture was dropped onto a blue emission mini-LED chip and then thermally cured for 2 h at 150 °C in an oven. For the light penetration experiment, pork was selected and cut into slices with a thickness of 0.5 cm each. Then the mini-LED was loaded with the driving voltage of 2.8 V and current of 150 mA. The lighted mini-LED and meat slices were set in a FluoroMax-4 spectrophotometer (HORIBA) to let the emitted light of LED penetrate the meat slice. The detector was using PMT-980, and we set the target wavelength of 710 nm with the slit of 1 nm.

RESULTS AND DISCUSSION

The microemulsion method was applied to synthesize Cs_4PbI_6 microcrystals. To provide more I^- and thus enhance the formation of Cs_4PbI_6, we first tuned the ratio of ZnI_2 to the PbI_2

precursor with the parameter $x = ZnI_2/(ZnI_2 + PbI_2)$. Based on the XRD patterns shown in **Figure 1**a, the main phase in these samples changes from δ-$CsPbI_3$ to Cs_4PbI_6 and finally turns to be CsI with the increase in x. The elemental ratios of Pb:I in $CsPbI_3$ and Cs_4PbI_6 are significantly different. The reactants used were Cs- oleate, PbI_2, and ZnI_2. When less ZnI_2 was added, the system tended to produce $CsPbI_3$ with a higher ratio of Pb:I. When more ZnI_2 was added ($x = 0.67$), the nominal Pb:I ratio was 1:6, and the content of the Cs_4PbI_6 increased. However, when excess ZnI_2 was added, the system tended to produce CsI. Consequently, the additive ZnI_2 played an important role in governing the reaction balance to form Cs_4PbI_6.

Scanning electron microscopy (SEM) images were obtained to further evaluate the phase transformation in these samples, as shown in Figs. 1b–f. The sample of $x = 57\%$ shows an almost uniform hexagonal morphology, which is close to the typical morphology of the Cs_4PbI_6 crystals. The sample with $x = 100\%$ contains irregular small rock salt particles of CsI, while samples with $x = 0$–50% contain many rod-shaped particles, corresponding to δ-$CsPbI_3$. The trend of the Cs_4PbI_6 content in these samples at different x is summarized in Figure 1g. Based on these results, we selected the $x = 57\%$ precursor as the most suitable recipe for further optimization.

The different acidic environments controlled by y = OAm/(OAm + OA), (OAm: oleylamine, OA: oleic acid) was tested to investigate the synthetic conditions to achieve high-quality monophasic Cs_4PbI_6. According to the XRD patterns shown in **Figure S1**, we can find that the Cs_4PbI_6 content in these samples keeps increasing with y and reaches a maximum when y is 100% (Figure 1h). The corresponding SEM images in **Figure S2** confirms that the sample with $y = 100\%$ contains highly uniform hexagon particles. Hence, the prescription of $x = 57\%$ in a basic environment should be the most suitable condition for the fabrication of Cs_4PbI_6.

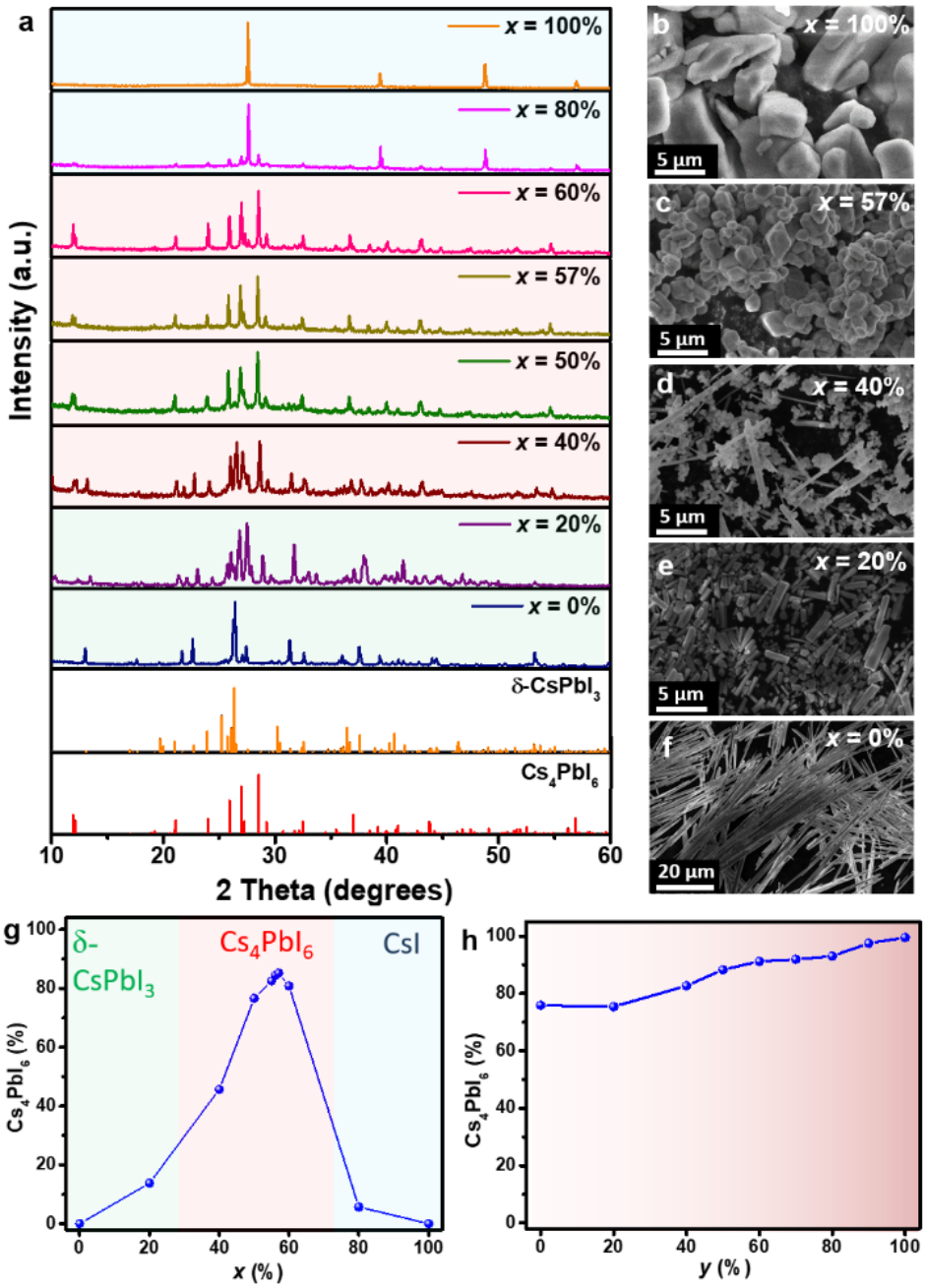

Figure 1. Optimization of the synthesis process for Cs_4PbI_6. (a) XRD patterns of the samples synthesized with different values of $x = ZnI_2/(ZnI_2 + PbI_2)$ with the theoretical patterns of δ-$CsPbI_3$ and Cs_4PbI_6. SEM images of the samples synthesized with x values of (b) 100%, (c) 57%, (d) 40%, (e) 20%, and (f) 0%. The percentage of the Cs_4PbI_6 phase in the products with the different value of (g) x = $ZnI_2/(ZnI_2 + PbI_2)$ and (h) y =OAm/(OAm + OA).

To explore whether other metal iodide additives can help in the formation of Cs_4PbI_6, we tested LiI, KI, NiI_2, CoI_2, and SnI_2 in synthesis. According to the XRD patterns of the products in **Figure 2**a, all these metal iodides can lead to the formation of Cs_4PbI_6, but the ZnI_2-containing system results in the highest yield of Cs_4PbI_6. During the synthesis, the metal iodides partially provided the source of iodine anions partially.[28] Therefore, the lower the dissociation energy of the metal iodide, the more iodide ions it can provide, and the easier the formation of the Cs_4PbI_6 microcrystals. The dissociation energy of each metal iodide at 298 K is shown in Figure 2b. According to the relation of the Cs_4PbI_6 content with the dissociation energy shown in Figure 2c, ZnI_2 has the lowest dissociation energy for providing extra iodide ions. Therefore, it can lead to the highest purity of the Cs_4PbI_6 product.

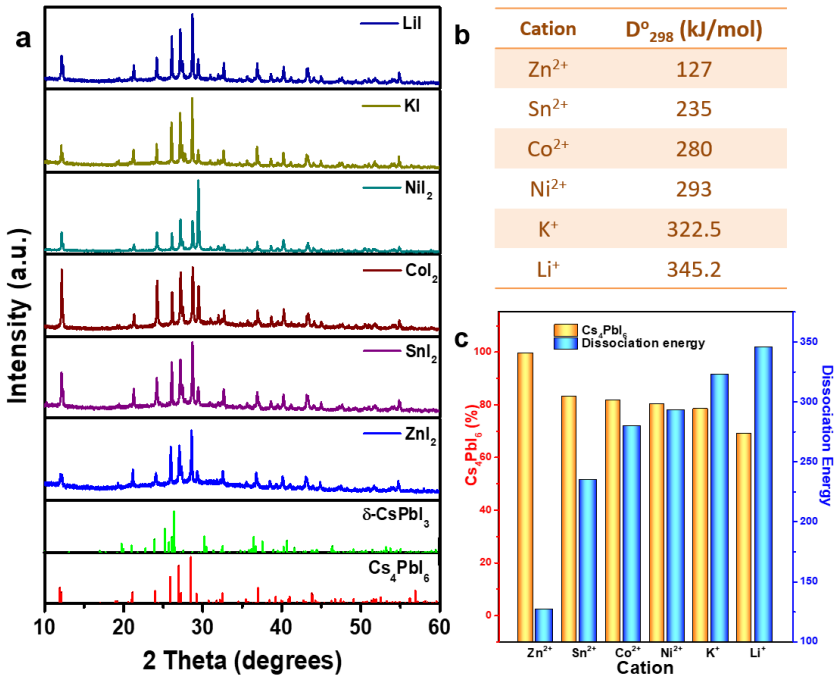

Figure 2. Characterization of Cs_4PbI_6 synthesized with different metal iodide additives. (a) XRD patterns of the products. (b) Dissociation energy of the metal iodide salts. (c) Cs_4PbI_6 content in the products compared with the dissociation energy of different metal iodide salts in the precursors.

To examine the exact phase compositions of the optimal Cs_4PbI_6 with x = 57% and y = 100% (see the definitions for x and y above), we discussed the local structural information in detail. Synchrotron XRD and Rietveld refinement were performed, and the results are shown in **Figure 3**a and Table S1. According to the well-matched fitting curve, the as-synthesized specimen has a similar structure to Cs_4PbBr_6, which is hexagonal with unit cell parameters of a = 14.58 Å and c = 18.34 Å, as shown in Figure 3b. The multiphase Rietveld refinement of this product shows that Cs_4PbI_6 is the main phase (~99.5%), with 0.5% δ-$CsPbI_3$ as the only impurity. The latter has an orthorhombic structure with a = 10.43 Å and c = 17.76 Å. This result proves that our Cs_4PbI_6 sample is very close to the pure phase. **Figures S3**a–d show the SEM image and EDS elemental mapping of Cs, Pb, and I from this optimal Cs_4PbI_6 specimen, from which we can ensure the uniform distribution of each element.

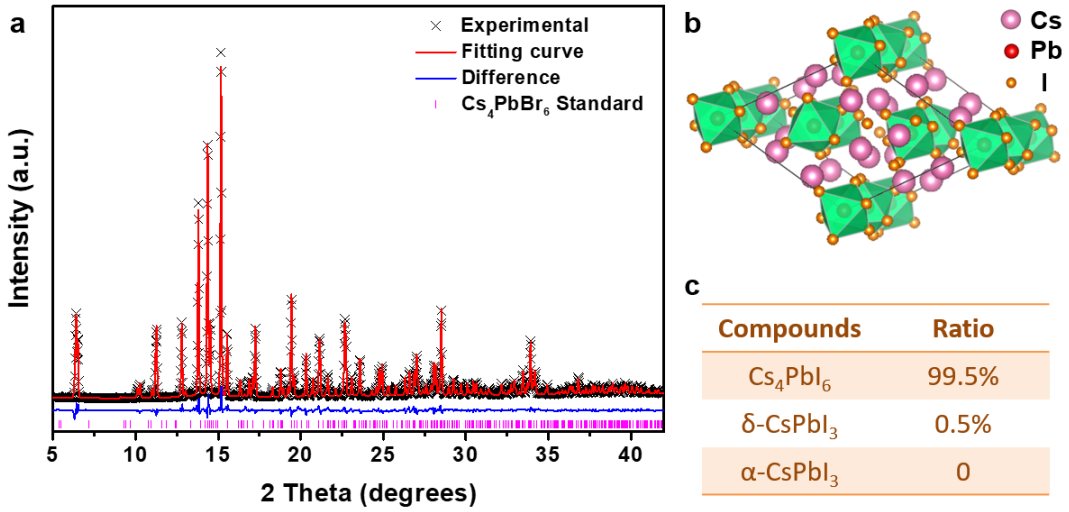

Figure 3. Phase characterization of the as-synthesized Cs_4PbI_6. (a) Rietveld refined synchrotron XRD (beamline energy 20 keV) pattern of Cs_4PbI_6. (b) Crystal structure of Cs_4PbI_6. (c) Composition of the specimen and corresponding ratio of Cs_4PbI_6 : $CsPbI_3$ from the Rietveld refinement.

XRD refinement did not catch the α-$CsPbI_3$ phase in the sample, which has a cubic unit cell with a = 6.41 Å. However, this observation cannot rule out the possible existence of very small α-$CsPbI_3$ nanocrystallites (NCs) embedded in Cs_4PbI_6 crystals. HRTEM images may readily reveal these NCs.

TEM images show that the specimen contains Cs_4PbI_6 crystals (confirmed below) as the major phase with some short nanorods. The latter was relatively stable under electron beam irradiation, and the structure was orthorhombic δ-$CsPbI_3$, as confirmed by the HRTEM images (**Figure S4**). Cs_4PbI_6 is beam-sensitive and a low dose of electrons must be applied to avoid decomposition of the crystals in a few minutes. Low-magnification TEM images show many dark dots inside the particles, as shown in the inset of Figure 4a. These dark dots, as shown below, are embedded α-$CsPbI_3$ NCs with an average diameter of ~5 nm. The strong image contrast is caused by the large difference in the density of the heaviest element Pb between $CsPbI_3$ and Cs_4PbI_6. The whole structure of the particles looks like raisin bread. We then simplified the name of α-$CsPbI_3$ embedded Cs_4PbI_6 to 'raisin bread'-Cs_4PbI_6 or RB-Cs_4PbI_6.

Figure 4a shows an HRTEM image of an RB–Cs_4PbI_6 particle. The fringes covering a large area, marked A, have a d-spacing of 3.32 Å, which can be indexed to the {131} atomic planes of Cs_4PbI_6 (theoretical $d_{(131)}$ = 3.31 Å). A few dark dots were visible and showed atomic lattice fringes when a principal crystallographic orientation is parallel to the electron beam. A good example is an NC at the top-left corner with three independent d-spacings marked B, C, and D. These d-spacings have dimensions of d_B = 2.83 Å, d_C = 2.89 Å, and d_D = 3.29 Å, which are assigned to the (102), (10$\bar{2}$) and (200) planes of the α-$CsPbI_3$ phase, respectively (theoretical values of $d_{(102)}$ = $d_{(10\text{-}2)}$ = 2.87 Å and $d_{(200)}$ = 3.21 Å). The interplanar angles of ∠(102, 10$\bar{2}$) and ∠(102, 200) were 129.5° and 64.28° with the corresponding theoretical values of 126.9° and 63.43°, respectively.

These *d*-spacings of the small crystallite cannot be indexed to either hexagonal Cs_4PbI_6 or orthorhombic δ-$CsPbI_3$, thus confirming the α-$CsPbI_3$ phase, although small distortion from the bulk crystal structure is possible. In Figure 4b, the fringes of both the parent Cs_4PbI_6 crystal (E) and α-$CsPbI_3$ NCs (F, G, H) are observed at the edge of a particle.

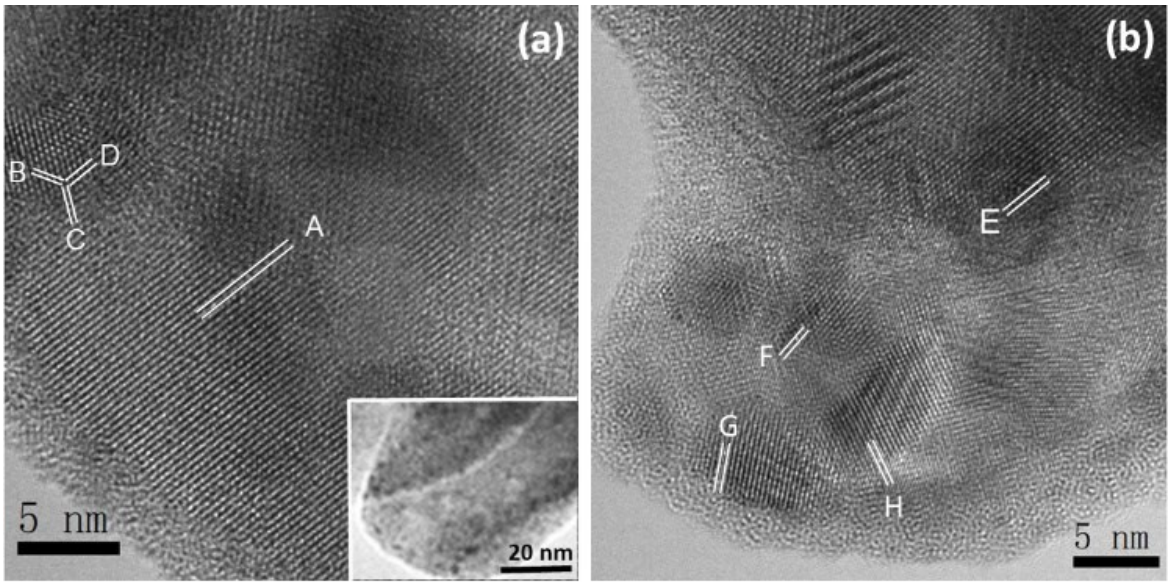

Figure 4. HRTEM images of an RB-Cs_4PbI_6 particle. (a) HRTEM image showing the (131) fringes of the Cs_4PbI_6 structure (A) and three *d*-spacings of an embedded nanocrystallite, which can be indexed to the cubic α-$CsPbI_3$ structure, B: (102), C: (10$\bar{2}$), and D: (200). The inset shows a low-magnification TEM image of the particle with a raisin bread-like structure. (b) HRTEM image of an edge area in the RB-Cs_4PbI_6 particle. The *d*-spacing of E is indexed to (131) of Cs_4PbI_6. Other d-spacings are indexed to α-$CsPbI_3$, F: (200), and G and H: (210).

Solid-state nuclear magnetic resonance (ssNMR), a sensitive analytical technique to characterize the local structure, has been widely applied to probe the local structure of perovskites.[29-38] In particular, ^{133}Cs ssNMR can precisely characterize the coordination

environment of cesium cations in the perovskite lattice.[39-47] ^{133}Cs has 100% natural abundance, and its nucleus has a spin quantum number of 7/2. The interaction between the quadrupole moment of ^{133}Cs nuclei and the electric field gradient (EFG) at the nuclear site is characterized by the quadrupole coupling constants (QCC) and the asymmetry parameter (η_Q). The chemical shift is a good spectral marker for a particular species, and QCC and η_Q reveal the charge symmetry at the nuclear site. A highly symmetric charge distribution at a nuclear site would result in a small QCC, and a vanishing η_Q indicates the presence of the axial symmetry of the EFG tensor. In the present work, we employed ^{133}Cs NMR to probe the various crystalline phases in Cs_4PbI_6.

As shown in **Figure 5**a–d, the ^{133}Cs ssNMR spectra of the as-synthesized crystals were acquired, from which the NMR parameters were extracted via simulations carried out by using DMFit2019.[48] As shown in Table S2, the x = 0 sample, which corresponds to pure δ-$CsPbI_3$, underwent a ^{133}Cs chemical shift of 256.4 ppm, which is consistent with the literature data.[14] For the x = 20% and 50% samples, two additional signals at 273 and 427 ppm emerged at the expense of the signal intensity of δ-$CsPbI_3$. Based on Rietveld analysis of the corresponding XRD patterns (Figure 5e), the larger signal at 273 ppm is assigned to Cs_4PbI_6. To our knowledge, these ^{133}Cs NMR data were the first to be reported for Cs_4PbI_6. On the other hand, the appearance of the signal at approximately 427 ppm is remarkable. Furthermore, the intensity of this extraordinarily deshielded signal increased with x, indicating that it originated from a crystalline phase of the ternary system of Cs-Pb-I. Based on the HRTEM results, we tentatively assigned the X-phase to nanoscale α-$CsPbI_3$ formed within the host of Cs_4PbI_6 ($CsPbI_3$ embedded in Cs_4PbI_6).

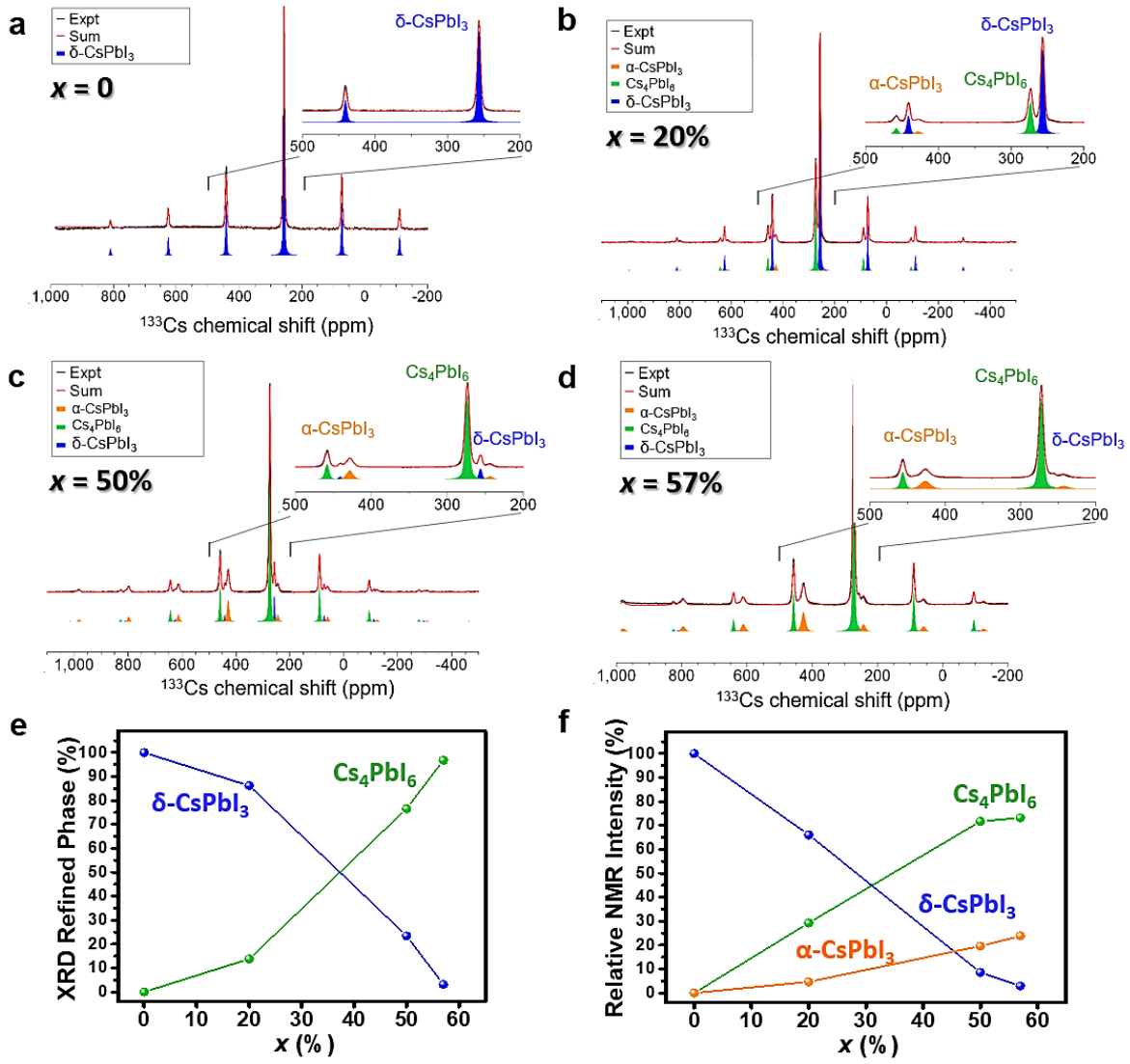

Figure 5. ssNMR of the achieved samples with different values of x = ZnI_2/(ZnI_2 + PbI_2). The ssNMR spectra of (a) x = 0, (b) x = 20%, (c) x = 50%, and (d) x = 57%. (e) Ratio of Cs_4PbI_6 and δ-$CsPbI_3$ based on XRD. (f) Relative NMR intensity of Cs_4PbI_6, α-$CsPbI_3$, and δ-$CsPbI_3$.

To prove that the luminescent process of RB-Cs_4PbI_6 is from the embedded $CsPbI_3$ nanoparticles in the Cs_4PbI_6, we analyzed their optical properties. The RT PLE and PL spectra of RB-Cs_4PbI_6 are shown in **Figure 6**a. The RB-Cs_4PbI_6 exhibited three photoluminescence excitation peaks at 348 and 400 nm and a broadband excitation ranging from 430 nm to over 650

nm with a maximum at 460 nm upon monitoring at 698 nm. Based on the previous report, the 348 nm peak is associated with the excitonic transition in Cs_4PbI_6.[27] In our measurements, the whole excitation spectrum is below the bandgap energy of Cs_4PbI_6. Thereby, the small peak at approximately 400 nm refers to the absorption associated with states in the energy band gap, from which it transfers to the emission centers. At the present stage, we can consider that they are self-trapped exciton and/or Pb-trapped excitons or transition in Pb^{2+} ion. The excitation band between 450–650 nm corresponds to the direct absorption of the luminescence centers. In the PL spectra at RT, a red-NIR narrowband emission peaked at 698 nm, which does not depend on the excitation wavelength, was observed. The full width at half maximum (FWHM) of this narrow emission is only 34 nm, which is very similar to that of $CsPbI_3$ NCs. The PLQY of this sample is about 23.2% and performed good stability to remain 71% original intensity after the test at 85 °C and 85% moisture for 96 h (Figure 6b).

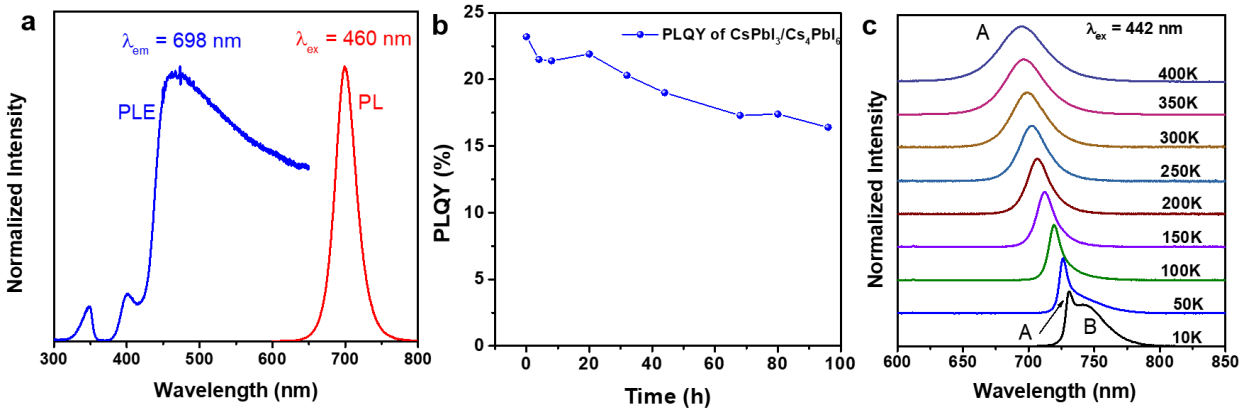

Figure 6. Emission properties of the as-synthesized RB-Cs_4PbI_6. (a) The room temperature (RT) photoluminescence excitation (PLE) spectrum upon emission at 698 nm and PL spectrum upon excitation at 460 nm of RB-Cs_4PbI_6. (b) The PLQY of the as-synthesized RB-Cs_4PbI_6 after the test

at 85 °C and 85% moisture for a different time. (c) Temperature dependence of normalized luminescence spectra under CW excitation with 442 nm at the temperature range of 10–400 K.

The temperature-dependent PL spectra at the temperature range of 10–400 K upon continuous wave (CW) excitation at 442 nm were obtained to further explore the emission behavior. As shown in Figure 6b, the two overlapping bands were observed at 730 and 740 nm at 10 K, denoted as A and B bands, respectively. When the temperature increased, a shift towards lower wavelength (higher energies) and emission broadening was observed for the A band. The B emission band decreased compared with the A band and quenched at 100 K. The different PL decay time (**Figure S5**), time-resolved emission spectra at 10 K (**Figure S6**), and the relative emission intensities of bands A and B under different excitation powers (**Figure S7**) further supported that band A is associated with the excitonic emission related to the α-$CsPbI_3$ nanoparticles, and band B was caused by trap states.

To confirm the inference that the band A is associated with the embedded α-$CsPbI_3$, pressure-dependent PL spectra were also obtained. **Figure 7** shows the pressure-dependent luminescence of Cs_4PbI_6 upon excitation at 442 nm with a pressure range up to 100 kbar. The narrowband A emission was observed with a maximum at 700 nm up to 10 kbar, while a significant change of emission was observed under high pressure. The broadband emission (denoted as C band) with maximum wavelength at 750 nm was observed at 13 kbar and shifted towards higher energies (lower wavelength) with a further increase in pressure. This change in emission spectra indicates the phase transition between 10 kbar and 13 kbar. The broadband emission spectrum (C band) at high pressure is possibly associated with emission from a deep local state in Cs_4PbI_6. The

position of the maximum luminescence wavelength before and after phase transition is shown in Figure 7b.

The change in position of the maximum luminescence is negligible before phase transition (blue dots). After phase transition, a large shift is observed, and when reaching the pressure of 60 kbar, the shift rate decreased under higher pressure. The luminescence decay profiles before and after phase transition are shown in Figures 7c and d, respectively. The decay profile for the luminescence before phase transition is in the ns range and does not change with the pressure up to 10 kbar. After phase transition at 13–100 kbar, the luminescence decay is in the μs range and was significantly shortened with increasing pressure. Figure 7e shows the images of Cs_4PbI_6 at high hydrostatic pressures of 2, 20, 40, 60, and 80 kbar.

The color of the investigated sample changed from white under 2 kbar (before phase transition), bright yellow under 20 kbar (after phase transition), and red and dark red under high pressures. The color change is associated with the change in the absorption of $CsPbI_3$ nanoparticles. Observed pressure shift of the absorption edge towards lower energy indicates a decrease in the energy gap in $CsPbI_3$.

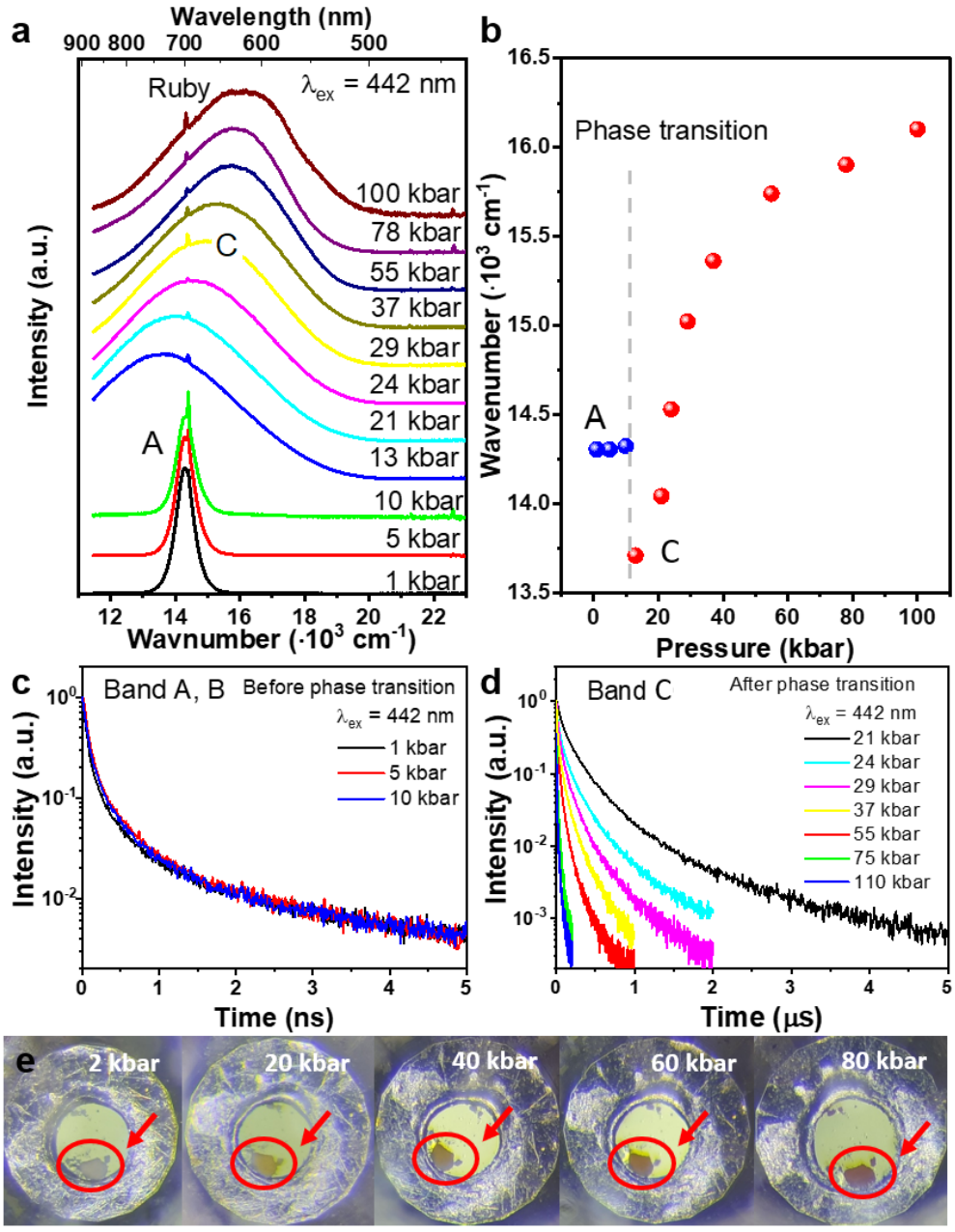

Figure 7. Pressure-dependent luminescent performance of RB-Cs4PbI6. (a) Pressure dependence of luminescence spectra and (b) the position of the maximum of luminescence before (blue dots) and after (red dots) phase transition. The emission peaks around 700 nm in (a) are from the additional ruby for the pressure indicator. Luminescence decay profiles in the (c) 5 ns range before phase transition and in the (d) 5 μs range after a phase transition of Cs4PbI6 under excitation with 442 nm. (e) Image of RB-Cs4PbI6 at high hydrostatic pressures of 2, 20, 40, 60, and 80 kbar.

High-pressure experiments clearly show that in this material, we can distinguish the two different emissions from α-$CsPbI_3$ nanoparticles at normal pressure and from Cs_4PbI_6 at high pressure. Based on the combination of the result of structural characterization and spectroscopic results proved that the strong red-NIR emission at room temperature and atmospheric pressure originated from the embedded $CsPbI_3$ nanoparticles in the RB-Cs_4PbI_6.

The achieved RB-Cs_4PbI_6 were applied to mini-LED chips to check their potential for future application. As shown in **Figure 8**a, the fabricated mini-LEDs present the emission centered at 710 nm with an output power of 0.56 mW, where 9 × 5 mils mini-LED chips were used. Although some part of the emission by this sample covered the deep-red region, the emission peak and most parts are in the NIR region. Thereby, we treat the obtained mini-LED with such narrow emission as the NIR mini-LED. To test the possibility of achieved NIR mini-LEDs in the biological application, we used slices of meat to simulate human tissue for the penetration experiment. Exactly 20.3% of the original intensity of light penetration remained after transferring the first meat slice with a thickness of 0.5 cm. With increasing meat slice thickness, the light penetration was limited to the thickness of 1.5 cm and disappeared upon reaching 2.0 cm, as shown in Figure 8b. Hence, the penetration ability of this NIR mini-LED for meat slices indicating the great potential of the RB-Cs_4PbI_6 for biological applications.

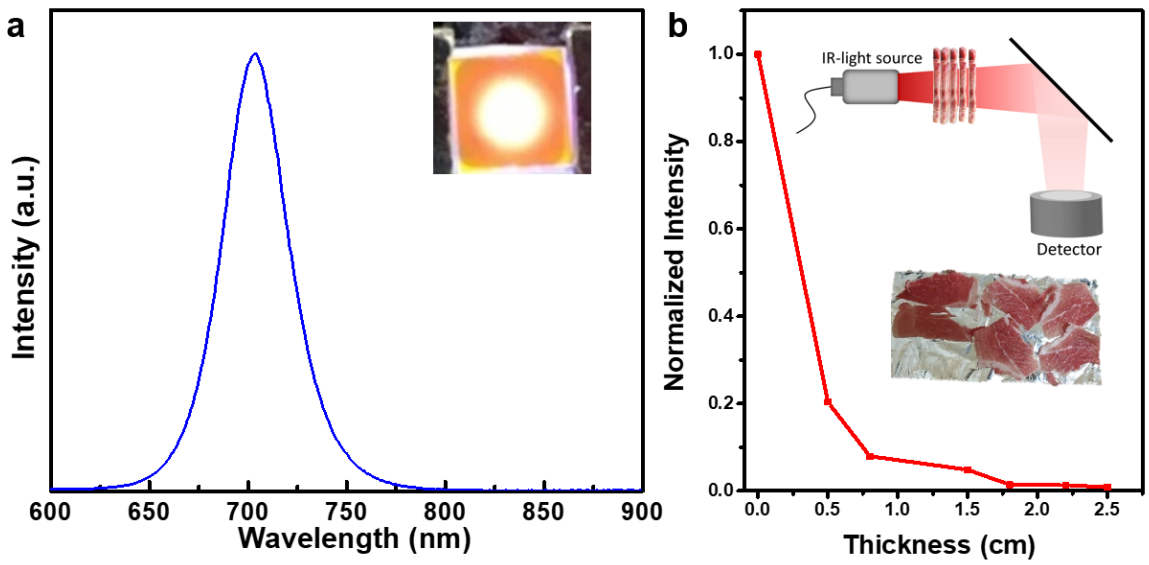

Figure 8. Application of RB-Cs_4PbI_6 in near-infrared light-emitting diodes. (a) Infrared light-emitting diode fabricated with the RB-Cs_4PbI_6 synthesized at x = 57% and y = 100%. The insert image shows the photograph of its working status. (b) Trend of emission intensity with different penetration depths of meat slice.

CONCLUSIONS

In summary, we successfully optimized the synthesis process for achieving the Cs_4PbI_6 with the optimization of additional ZnI_2 in the low-temperature synthesis process. Results show that the lower the dissociation energy of the additional metal iodide, the easier the extra I^- for driving the formation of Cs_4PbI_6. Based on XRD and HRTEM results, we ensured the sample with x = 57% and y = 100% is the composite structure of Cs_4PbI_6 embedded with α-$CsPbI_3$ nanoparticles. The overall structure is raisin bread-like according to these results. Moreover, a NIR mini-LED for the biological application was successfully fabricated by as-synthesized Cs_4PbI_6 crystals. The results of this study will provide a basis for further study on zero-dimensional perovskite for wider applications

ASSOCIATED CONTENT

Supporting Information. The Supporting Information is available free of charge on the ACS Publications website at DOI: 10.1021/acsenergylett.XXXXXXX.

XRD patterns and SEM images of the samples synthesized with different *y* values, EDS elemental mapping, further ssNMR information, HRTEM image, further discussion of temperature-dependent PL properties.

AUTHOR INFORMATION

Corresponding Authors

wzhou@st-andrews.ac.uk (W. Z. Zhou)

rsliu@ntu.edu.tw (R. S. Liu)

Notes

The authors declare no competing financial interest.

ACKNOWLEDGMENT

This work was financially supported by the Advanced Research Center of Green Materials Science and Technology from The Featured Area Research Center Program within the framework of the Higher Education Sprout Project by the Ministry of Education (107L9006), the Ministry of Science and Technology in Taiwan (Contracts MOST 109-2113-M-002-020-MY3, MOST 107-2113-M-002-008-MY3, MOST 110-2923-M-002-017-MY3, MOST 107-2923-M-002-004-MY3 and MOST 107-3017-F-002-001), the National Science Center Poland Grant Opus (Nos.

2016/23/B/ST3/03911 and No. 2019/33/B/ST3/00406), and the National Center for Research and Development Poland Grant (No. PL-TW/VIII/1/2021).

REFERENCES

(1) Jeon, N. J.; Noh, J. H.; Yang, W. S.; Kim, Y. C.; Ryu, S.; Seo, J.; Seok, S. I. Compositional Engineering of Perovskite Materials for High-Performance Solar Cells. *Nature* **2015,** *517*, 476–480.

(2) Forgács, D.; Gil-Escrig, L.; Pérez-Del-Rey, D.; Momblona, C.; Werner, J.; Niesen, B.; Ballif, C.; Sessolo, M.; Bolink, H. J. Efficient Monolithic Perovskite/Perovskite Tandem Solar Cells. *Adv. Energy Mater.* **2017,** *7*, 1602121.

(3) Zhang, F.; Zhong, H.; Chen, C.; Wu, X.-g.; Hu, X.; Huang, H.; Han, J.; Zou, B.; Dong, Y. Brightly Luminescent and Color-Tunable Colloidal $CH_3NH_3PbX_3$ (X = Br, I, Cl) Quantum Dots: Potential Alternatives for Display Technology. *ACS Nano* **2015,** *9*, 4533–4542.

(4) Wang, H. C.; Wang, W.; Tang, A. C.; Tsai, H. Y.; Bao, Z.; Ihara, T.; Yarita, N.; Tahara, H.; Kanemitsu, Y.; Chen, S.; Liu, R. S. High‐Performance $CsPb_{1-x}Sn_xBr_3$ Perovskite Quantum Dots for Light‐Emitting Diodes. *Angew. Chem.* **2017,** *129*, 13838–13842.

(5) Bao, Z.; Wang, W.; Tsai, H. Y.; Wang, H. C.; Chen, S.; Liu, R. S. Photo-/Electro-Luminescence Enhancement of $CsPbX_3$ (X = Cl, Br, or I) Perovskite Quantum Dots via Thiocyanate Surface Modification. *J. Mater. Chem. C* **2019,** *8*, 1065–1071.

(6) Bao, C.; Yang, J.; Bai, S.; Xu, W.; Yan, Z.; Xu, Q.; Liu, J.; Zhang, W.; Gao, F. High Performance and Stable All‐Inorganic Metal Halide Perovskite‐Based Photodetectors for Optical Communication Applications. *Adv. Mater.* **2018**, 1803422.

(7) Dou, L.; Yang, Y. M.; You, J.; Hong, Z.; Chang, W. H.; Li, G.; Yang, Y. Solution-Processed Hybrid Perovskite Photodetectors with High Detectivity. *Nat. Commun.* **2014,** *5*, 5404.

(8) Kovalenko, M. V.; Protesescu, L.; Bodnarchuk, M. I. Properties and Potential Optoelectronic Applications of Lead Halide Perovskite Nanocrystals. *Science* **2017,** *358*, 745–750.

(9) Huang, S.; Li, Z.; Wang, B.; Zhu, N.; Zhang, C.; Kong, L.; Zhang, Q.; Shan, A.; Li, L. Morphology Evolution and Degradation of $CsPbBr_3$ Nanocrystals under Blue Light-Emitting Diode Illumination. *ACS Appl. Mater. Interfaces* **2017,** *9*, 7249–7258.

(10) Bao, Z.; Wang, H. C.; Jiang, Z. F.; Chung, R. J.; Liu, R. S. Continuous Synthesis of Highly Stable Cs_4PbBr_6 Perovskite Microcrystals by a Microfluidic System and Their Application in White-Light-Emitting Diodes. *Inorg. Chem.* **2018,** *57*, 13071–13074.

(11) Akkerman, Q. A.; Abdelhady, A. L.; Manna, L. Zero-Dimensional Cesium Lead Halides: History, Properties, and Challenges. *J. Phys. Chem. Lett.* **2018,** *9*, 2326–2337.

(12) Bi, C.; Wang, S.; Wen, W.; Yuan, J.; Cao, G.; Tian, J. Room-Temperature Construction of Mixed-Halide Perovskite Quantum Dots with High Photoluminescence Quantum Yield. *J. Phys. Chem. C* **2018,** *122*, 5151–5160.

(13) Chen, Y. M.; Zhou, Y.; Zhao, Q.; Zhang, J.-Y.; Ma, J.-P.; Xuan, T.-T.; Guo, S.-Q.; Yong, Z.-J.; Wang, J.; Kuroiwa, Y. $Cs_4PbBr_6/CsPbBr_3$ Perovskite Composites with Near-Unity Luminescence Quantum Yield: Large-Scale Synthesis, Luminescence and Formation Mechanism, and White Light-Emitting Diode Application. *ACS Appl. Mater. Interfaces* **2018,** *10*, 15905–15912.

(14) Chen, D.; Wan, Z.; Chen, X.; Yuan, Y.; Zhong, J. Large-scale Room-Temperature Synthesis and Optical Properties of Perovskite-Related Cs_4PbBr_6 Fluorophores. *J. Mater. Chem. C* **2016,** *4*, 10646–10653.

(15) Chen, X.; Zhang, F.; Ge, Y.; Shi, L.; Huang, S.; Tang, J.; Lv, Z.; Zhang, L.; Zou, B.; Zhong, H. Centimeter - Sized Cs_4PbBr_6 Crystals with Embedded $CsPbBr_3$ Nanocrystals Showing Superior Photoluminescence: Nonstoichiometry Induced Transformation and Light - Emitting Applications. *Adv. Funct. Mater.* **2018,** *28*, 1706567.

(16) Wang, W.; Wang, D.; Fang, F.; Wang, S.; Xu, G.; Zhang, T. $CsPbBr_3/Cs_4PbBr_6$ Nanocomposites: Formation Mechanism, Large-Scale and Green Synthesis, and Application in White Light-Emitting Diodes. *Cryst. Growth Des.* **2018,** *18*, 6133–6141.

(17) Su, M.; Fan, B.; Li, H.; Wang, K.; Luo, Z. Hydroxyl Terminated Mesoporous Silica-Assisted Dispersion of Ligand-Free $CsPbBr_3/Cs_4PbBr_6$ Nanocrystals in Polymer for Stable White LED. *Nanoscale* **2019,** *11*, 1335–1342.

(18) Bao, Z.; Tseng, Y. J.; You, W.; Zheng, W.; Chen, X.; Mahlik, S.; Lazarowska, A.; Lesniewski, T.; Grinberg, M.; Ma, C.; Sun, W.; Zhou, W.; Liu, R. S.; Attfield, J. P. Efficient Luminescence from $CsPbBr_3$ Nanoparticles Embedded in Cs_4PbBr_6. *J. Phys. Chem. Lett.* **2020,** *11*, 7637–7642.

(19) Steele, J. A.; Lai, M.; Zhang, Y.; Lin, Z.; Hofkens, J.; Roeffaers, M. B.; Yang, P. Phase Transitions and Anion Exchange in All-Inorganic Halide Perovskites. *Acc. Mater. Res.* **2020,** *1*, 3–15.

(20) Marronnier, A.; Roma, G.; Boyer-Richard, S.; Pedesseau, L.; Jancu, J.-M.; Bonnassieux, Y.; Katan, C.; Stoumpos, C. C.; Kanatzidis, M. G.; Even, J. Anharmonicity and Disorder in the Black Phases of Cesium Lead Iodide Used for Stable Inorganic Perovskite Solar Cells. *ACS Nano* **2018,** *12*, 3477–3486.

(21) Dastidar, S.; Hawley, C. J.; Dillon, A. D.; Gutierrez-Perez, A. D.; Spanier, J. E.; Fafarman, A. T. Quantitative Phase-Change Thermodynamics and Metastability of Perovskite-Phase Cesium Lead Iodide. *J. Phys. Chem. Lett.* **2017,** *8*, 1278–1282.

(22) Frolova, L. A.; Anokhin, D. V.; Piryazev, A. A.; Luchkin, S. Y.; Dremova, N. N.; Stevenson, K. J.; Troshin, P. A. Highly Efficient All-Inorganic Planar Heterojunction Perovskite Solar Cells Produced by Thermal Coevaporation of CsI and PbI_2. *J. Phys. Chem. Lett.* **2017,** *8*, 67–72.

(23) Burwig, T.; Fränzel, W.; Pistor, P. Crystal Phases and Thermal Stability of Co-Evaporated $CsPbX_3$ (X= I, Br) Thin Films. *J. Phys. Chem. Lett.* **2018,** *9*, 4808–4813.

(24) Christians, J. A.; Miranda Herrera, P. A.; Kamat, P. V. Transformation of the Excited State and Photovoltaic Efficiency of $CH_3NH_3PbI_3$ Perovskite Upon Controlled Exposure to Humidified Air. *J. Am. Chem. Soc.* **2015,** *137*, 1530–1538.

(25) Conings, B.; Drijkoningen, J.; Gauquelin, N.; Babayigit, A.; D'Haen, J.; D'Olieslaeger, L.; Ethirajan, A.; Verbeeck, J.; Manca, J.; Mosconi, E. Intrinsic Thermal Instability of Methylammonium Lead Trihalide Perovskite. *Adv. Energy Mater.* **2015,** *5*, 1500477.

(26) Eperon, G. E.; Stranks, S. D.; Menelaou, C.; Johnston, M. B.; Herz, L. M.; Snaith, H. J. Formamidinium Lead Trihalide: A Broadly Tunable Perovskite for Efficient Planar Heterojunction Solar Cells. *Energy Environ. Sci.* **2014,** *7*, 982–988.

(27) Liu, N.; Sun, R.; Wang, L.; Ji, Y.; Li, N.; Cao, B.; Zhang, Y. Unexpected Red Emission from Cs_4PbI_6 Nanocrystals. *Journal of Materials Chemistry A* **2020,** *8*, 5952–5958.

(28) Dey, A.; Ye, J.; De, A.; Debroye, E.; Ha, S. K.; Bladt, E.; Kshirsagar, A. S.; Wang, Z.; Yin, J.; Wang, Y. State of the Art and Prospects for Halide Perovskite Nanocrystals. *ACS Nano* **2021**.

(29) Aebli, M.; Piveteau, L.; Nazarenko, O.; Benin, B. M.; Krieg, F.; Verel, R.; Kovalenko, M. V. Lead-Halide Scalar Couplings in ^{207}Pb NMR of $APbX_3$ Perovskites (A = Cs, Methylammonium, Formamidinium; X = Cl, Br, I). *Scientific reports* **2020,** *10*, 1–9.

(30) Askar, A. M.; Karmakar, A.; Bernard, G. M.; Ha, M.; Terskikh, V. V.; Wiltshire, B. D.; Patel, S.; Fleet, J.; Shankar, K.; Michaelis, V. K. Composition-Tunable Formamidinium Lead Mixed

Halide Perovskites via Solvent-Free Mechanochemical Synthesis: Decoding the Pb Environments Using Solid-State NMR Spectroscopy. *J. Phys. Chem. Lett.* **2018,** *9*, 2671–2677.

(31) Franssen, W. M.; Bruijnaers, B. J.; Portengen, V. H.; Kentgens, A. P. Dimethylammonium Incorporation in Lead Acetate Based $MAPbI_3$ Perovskite Solar Cells. *ChemPhysChem* **2018,** *19*, 3107–3115.

(32) Kubicki, D. J.; Prochowicz, D.; Hofstetter, A.; Péchy, P. t.; Zakeeruddin, S. M.; Grätzel, M.; Emsley, L. Cation Dynamics in Mixed-Cation $(MA)_x(FA)_{1-x}PbI_3$ Hybrid Perovskites from Solid-State NMR. *J. Am. Chem. Soc.* **2017,** *139*, 10055–10061.

(33) Kubicki, D. J.; Prochowicz, D.; Hofstetter, A.; Zakeeruddin, S. M.; Grätzel, M.; Emsley, L. Phase Segregation in Potassium-Doped Lead Halide Perovskites from 39K Solid-State NMR at 21.1 T. *J. Am. Chem. Soc.* **2018,** *140*, 7232–7238.

(34) Piveteau, L.; Aebli, M.; Yazdani, N.; Millen, M.; Korosec, L.; Krieg, F.; Benin, B. M.; Morad, V.; Piveteau, C.; Shiroka, T. Bulk and Nanocrystalline Cesium Lead-Halide Perovskites as Seen by Halide Magnetic Resonance. *ACS Cent. Sci.* **2020,** *6*, 1138–1149.

(35) Roiland, C.; Trippé-Allard, G.; Jemli, K.; Alonso, B.; Ameline, J.-C.; Gautier, R.; Bataille, T.; Le Polles, L.; Deleporte, E.; Even, J. Multinuclear NMR as A Tool for Studying Local Order and Dynamics in $CH_3NH_3PbX_3$ (X = Cl, Br, I) Hybrid Perovskites. *PCCP* **2016,** *18*, 27133–27142.

(36) Rosales, B. A.; Hanrahan, M. P.; Boote, B. W.; Rossini, A. J.; Smith, E. A.; Vela, J. Lead Halide Perovskites: Challenges and Opportunities in Advanced Synthesis and Spectroscopy. *ACS Energy Lett.* **2017,** *2*, 906–914.

(37) Rosales, B. A.; Men, L.; Cady, S. D.; Hanrahan, M. P.; Rossini, A. J.; Vela, J. Persistent Dopants and Phase Segregation in Organolead Mixed-Halide Perovskites. *Chem. Mater.* **2016,** *28*, 6848–6859.

(38) Sharma, S.; Weiden, N.; Weiss, A. ^{207}Pb and ^{205}Tl NMR on Perovskite Type Crystals $APbX_3$ (A = Cs, Tl, X = Br, I). *Zeitschrift fur Naturforschung A* **1987,** *42*, 1313–1320.

(39) Chen, Y.; Smock, S. R.; Flintgruber, A. H.; Perras, F. A.; Brutchey, R. L.; Rossini, A. J. Surface Termination of $CsPbBr_3$ Perovskite Quantum Dots Determined by Solid-State NMR Spectroscopy. *J. Am. Chem. Soc.* **2020,** *142*, 6117–6127.

(40) Karmakar, A.; Bernard, G. M.; Meldrum, A.; Oliynyk, A. O.; Michaelis, V. K. Tailorable Indirect to Direct Band-Gap Double Perovskites with Bright White-Light Emission: Decoding Chemical Structure Using Solid-State NMR. *J. Am. Chem. Soc.* **2020,** *142*, 10780–10793.

(41) Kubicki, D. J.; Prochowicz, D.; Hofstetter, A.; Zakeeruddin, S. M.; Grätzel, M.; Emsley, L. Phase Segregation in Cs-, Rb-and K-Doped Mixed-Cation $(MA)_x(FA)_{1-x}PbI_3$ Hybrid Perovskites from Solid-State NMR. *J. Am. Chem. Soc.* **2017,** *139*, 14173–14180.

(42) Kubicki, D. J.; Prochowicz, D.; Pinon, A.; Stevanato, G.; Hofstetter, A.; Zakeeruddin, S. M.; Grätzel, M.; Emsley, L. Doping and Phase Segregation in Mn^{2+}-and Co^{2+}-Doped Lead Halide Perovskites from ^{133}Cs and ^{1}H NMR Relaxation Enhancement. *Journal of Materials Chemistry A* **2019,** *7*, 2326–2333.

(43) Kubicki, D. J.; Saski, M.; MacPherson, S.; Gałkowski, K.; Lewiński, J.; Prochowicz, D.; Titman, J. J.; Stranks, S. D. Halide Mixing and Phase Segregation in Cs_2AgBiX_6 (X = Cl, Br, and I) Double Perovskites from Cesium-133 Solid-State NMR and Optical Spectroscopy. *Chem. Mater.* **2020,** *32*, 8129–8138.

(44) Lim, A.; Jeong, S.-Y. Twin Structure by ^{133}Cs NMR in Ferroelastic $CsPbCl_3$ Crystal. *Solid State Commun.* **1999,** *110*, 131 – 136.

(45) Lim, A. R.; Jeong, S.-Y. Ferroelastic Phase Transition and Twin Structure by ^{133}Cs NMR in a $CsPbCl_3$ Single Crystal. *Physica B: Condensed Matter* **2001,** *304*, 79–85.

(46) Prochowicz, D.; Yadav, P.; Saliba, M.; Kubicki, D. J.; Tavakoli, M. M.; Zakeeruddin, S. M.; Lewiński, J.; Emsley, L.; Grätzel, M. One-Step Mechanochemical Incorporation of An Insoluble Cesium Additive for High Performance Planar Heterojunction Solar Cells. *Nano Energy* **2018,** *49*, 523–528.

(47) Ran Lim, A.; Gyoo Kim, I. Phase Transition Study by Using ^{133}Cs and ^{207}Pb Nuclear Magnetic Resonance in a $CsPbCl_3$ Single Crystal. *J. Phys. Soc. Jpn.* **2004,** *73*, 475–479.

(48) Massiot, D.; Fayon, F.; Capron, M.; King, I.; Le Calvé, S.; Alonso, B.; Durand, J. O.; Bujoli, B.; Gan, Z.; Hoatson, G. Modelling One ‐ and Two ‐ Dimensional Solid ‐ State NMR Spectra. *Magn. Reson. Chem.* **2002,** *40*, 70 ‐ 76.

TOC GRAPHICS